Transient Stability Analysis and Improved Control Strategy of PMSG-based Grid-forming Wind Energy Conversion System Under Symmetrical Grid Fault

Hai Xie, Jun Yao, Wenwen He, Dong Yang, Sheng Gong, and Linsheng Zhao

***Abstract*—The transient synchronization characteristics and instability mechanism of the permanent magnet synchronous generator (PMSG)-based grid-forming wind energy conversion system (GFM-WECS) under symmetrical grid fault have received little attention to date. In this paper, considering the dynamics of DC-link voltage, the transient stability and an improved control strategy of PMSG-based GFM-WECS are studied in detail. Firstly, considering the dynamic interactions between the machine-side converter and the grid-side converter, the large-signal equivalent model of GFM-WECS is established. Furthermore, a novel Lyapunov function is derived to evaluate the transient stability margin and instability boundary of GFM-WECS during grid voltage sag. Additionally, the impacts of current-limitation control on the transient stability of GFM-WECS are revealed. Then, a stability evaluation index is proposed to evaluate the transient stability margin of GFM-WECS. Moreover, an improved control strategy is proposed to enhance the transient response characteristics and low voltage ride-through (LVRT) capability of GFM-WECS under symmetrical grid fault. Finally, simulations and experimental results are conducted to verify the effectiveness of the proposed control strategy.**

***Index Terms*—Grid-forming (GFM), permanent magnet synchronous generator (PMSG), wind energy conversion system (WECS), DC-link voltage, transient stability.**

NOMENCLATURE

A. Variables

α, γ	Impedance phase angle and stability evaluation index of transmission line considering current limitation
Δ, s, $1/s$	Difference, differential, and integral operators
δ, δ_0	Equivalent power angle and equivalent power angle at steady state
δ_s, δ_m	Stable equilibrium point and current limiter trigger angle
δ_{s1}, δ_{s2}	Stable and unstable equilibrium points under grid fault
θ_{GFM}, θ_{GFM}^{ref}	Phase angle and phase angle reference of grid-forming wind energy conversion system (GFM-WECS)
θ_g, θ_u	Phase angle of power grid and additional phase angle
θ_r, ω_r	Phase angle and angular speed of permanent magnet synchronous generator (PMSG)
ω_{SG}, ω_0	Angular frequency of synchronous generator (SG) and set point angular frequency
ω_{GFM}, ω_g, f, f_{min}, f_{max}	Angular frequency of GFM-WECS, angular frequency of power grid, frequency of GFM-WECS and its minimum and maximum values
C_{dc}, R_{dc}	DC-link capacitance and dissipative resistance of GFM-WECS
D_{dc}, D_{eq}	Damping of DC-link voltage and equivalent damping of GFM-WECS
D_{SG}	Damping coefficient of SG
E_{abc}, E_0, E_{gdq}^{ref}	Three-phase virtual back electromotive forces (EMFs), set point virtual back EMF, and d/q-axis virtual back EMF on grid side
H_g, k_s, k_t, k_i	Feedforward damping power gain, stator-side active loop modulation coefficient, transient damping modulation coefficient, and inertia modulation coefficient
I_{gdq}^{ref}, $\bar{I}_{gdq}^{ref}$, I_{max}	d/q-axis grid current reference, d/q-axis saturated line current reference, and the maximum current limitation amplitude
I_{sd}, I_{sd}^{ref}, I_{sq}, I_{sq}^{ref}	Stator-side d-axis current and its reference value, and q-axis current and its reference value

Manuscript received: May 22, 2024; revised: October 13, 2024; accepted: December 5, 2024. Date of CrossCheck: December 5, 2024. Date of online publication: January 20, 2025.

This work was supported by the National Natural Science Foundation of China (No. 51977019).

H. Xie, J. Yao (corresponding author), W. He, D. Yang, S. Gong, and L. Zhao are with the State Key Laboratory of Power Transmission Equipment Technology, School of Electrical Engineering, Chongqing University, Chongqing 400044, China (e-mail: 202211131293@stu.cqu.edu.cn; jyao@cqu.edu.cn; 1830756538@qq.com; ydcqu@stu.cqu.edu.cn; 20221101006@stu.cqu.edu.cn; zls410@stu.cqu.edu.cn).

DOI: 10.35833/MPCE.2024.000484

I_{sdq}, U_{sdq}, I_{gdq}, U_{gdq}	Stator-side d/q-axis current and voltage and grid-side d/q-axis current and voltage of GFM-WECS
J_{dc}, J_{eq}	Inertia of DC-link voltage and equivalent inertia of GFM-WECS
k_p, k_q	DC-link voltage synchronization gain and Q-E droop coefficient
L_g, L_f, C_f	Grid inductance, LC filter inductor, and LC filter capacitor
P_{D1}, P_{D2}	Dissipative power and feedforward damping power
P_{MPPT}, P_c	Maximum power point tracking (MPPT) power and instantaneous change of active power transfer limit
P_s, P_g, Q_g	Stator-side active power, grid-side active power, and grid-side reactive power
P_M, P_E	Mechanical power of prime mover and electromagnetic power of SG
P_{th}, Q_{th}, ΔP^{ref}	Threshold of active power, threshold of reactive power, and active power loop reference
P_{ig}, Q_{ig}	Grid-side active and reactive power when current limitation is reached
P_{ug}, Q_{ug}, $P_{ug,max}$	Grid-side active and reactive power when current limitation is not reached, and the maximum grid-side active power when current limitation is not reached
R_g, X_g, R_v	Grid resistance, grid reactance, and virtual resistance introduced by current limiter
T_{dc}	Time constant of low-pass filter
T_e	Electromagnetic power of PMSG
T_J, D_{SG}, ω_{SG}	Inertia time constant, damping coefficient and rotor angular speed of SG
U_{dc}, U_{dc0}, $U_{dc,min}$, $U_{dc,max}$	DC-link voltage, set point DC-link voltage of GFM-WECS, and the minimum and maximum DC-link voltage values
U_g, U_{pcc}, I_g	Grid voltage at fault location, voltage at point of common coupling (PCC), and grid current
$\boldsymbol{U}_g$, $\boldsymbol{U}_{pcc}$, $\boldsymbol{I}_g$	Vectors of grid voltage at fault location, voltage at PCC, and grid current
V_{cr1}, V_{cr2}	Critical values of designed Lyapunov function and conventional function
Y_{eq}, G_{eq}, B_{eq}	Equivalent admittance, conductance, and susceptance of transmission line
Z_g, Z_{grid}	Grid impedance and line impedance between fault location and grid

B. Subscripts

d/q	d/q-axis components
i, u	Components when current limitation is reached and not reached
r, s, g	Components of rotor-, stator-, and grid-side

I. Introduction

In the last decade, the penetration of large-scale distributed energy resources such as wind energy in the power grid has increased significantly [1]. Most wind resources are located in remote areas, resulting in a reduction in the short-circuit ratio (SCR) of the power grid, as well as a decrease in the grid-support capability of permanent magnet synchronous generator (PMSG)-based wind energy conversion system (WECS) [2]. Moreover, in power grids primarily dominated by synchronous generators (SGs), the transient stability issues have already been investigated thoroughly. By contrast, the stability issues in power-electronic-based power grids remain unclear and are much more complicated, especially under severe grid faults [3]. Therefore, the transient stability of WECS under symmetrical grid fault should be further studied.

So far, many studies have explored the stability issues of WECS under grid faults [4]-[6]. These studies are mainly divided into two aspects: the transient stability of grid-following WECS (GFL-WECS) and that of grid-forming WECS (GFM-WECS). Reference [7] indicates that both the absence of a stable equilibrium point (SEP) and a poor transient process will make GFL-WECS lose synchronization with the main grid. Reference [8] points out that the damping ratio of GFL-WECS is prone to decreasing due to a sudden drop of grid voltage. The decreased damping ratio will deteriorate the transient synchronization stability and even lead to the loss of synchronization. Reference [9] reveals that the control coefficients of phase-locked loop (PLL) have significant influence on the transient stability of GFL-WECS. Reference [10] demonstrates that the transient performance of GFM-WECS can be optimized by adjusting the damping coefficient and the order of the active power control loop properly. Besides, to determine the power angle dynamic characteristics of GFM-WECS, an unperturbed-result-based averaging method is proposed to obtain the explicit time-domain description of power angle dynamics in [11]. However, the aforementioned studies mainly focus on the transient behavior of the grid-side converter (GSC) during grid faults, while the influence of the machine-side converter (MSC) on the transient stability of GFM-WECS is neglected. In fact, the MSC will also deteriorate the synchronization stability under grid faults [2], [12]. Therefore, the influence of MSC on the transient stability of GFM-WECS under grid fault is worthy of further exploration.

Currently, the transient stability and control method of GFM-WECS have been preliminary studied in [13], [14]. Reference [13] reveals that the dynamics of DC-link voltage will decrease the transient stability margin of GFM-WECS. However, the transient instability mechanism of the GFM-WECS has not been further investigated. Reference [14] proposes a DC-link voltage synchronization control (DVSC) method, which can not only provide inertia and damping support for WECS, but also maintain the maximum power

point tracking (MPPT) control. Nevertheless, these control methods may not effectively ensure the low voltage ride-through (LVRT) capability of GFM-WECS under severe grid fault.

In addition, the impacts of current-limitation control on the transient stability of WECS are also rarely considered in above studies. Reference [15] indicates that existing current-limitation control methods can be classified into two categories, i.e., the instantaneous saturation limiter and the latched limiter. When the current limiter is triggered, the operating state of GFM-WECS will be changed immediately. Besides, [16] - [18] reveal that the power-characteristic curve under grid fault will change significantly, which may lead to transient instability. Particularly, when the fault current reaches the maximum current limitation magnitude, there is an instantaneous change in the active power transfer capability [19]. Moreover, the mechanism of the instantaneous change in the active power transfer capability has not been fully clarified and deserves further exploration.

In this paper, the transient stability of GFM-WECS with and without current limitation is studied. Then, considering the DC-link voltage dynamics, an improved control strategy is proposed to enhance the stability. The main contributions of this paper are summarized as follows.

1) A large-signal equivalent model of GFM-WECS is developed, and the dynamic interactions between MSC and GSC are analyzed. Then, the influences of key parameters such as the DC-link capacitance, transmission line admittance, and voltage sag on the transient synchronization behavior of the DC-link voltage under grid fault are investigated.

2) A novel Lyapunov function considering damping variation is designed for the transient stability analysis of GFM-WECS. Compared with the conventional Lyapunov function (CLF), the designed Lyapunov function (DLF) is more reliable.

3) The impacts of current limitation control on the transient stability of GFM-WECS are revealed. On this basis, a stability evaluation index is developed to evaluate the transient stability margin of GFM-WECS under current limitation.

4) Considering the linear relationship between the DC-link voltage and GFM-WECS, an improved control strategy involving MSC control and GSC control is proposed to enhance the stability. This strategy can ensure sufficient inertia and damping support for GFM-WECS during LVRT.

The remainder of this paper is organized as follows. In Section II, the modeling and transient synchronization behavior of GFM-WECS are presented. In Section III, the transient synchronization stability of GFM-WECS is analyzed via a DLF. In Section IV, the impacts of current limitation control on the transient stability of the GFM-WECS are revealed. In Section V, an improved control strategy is proposed, and simulations by MATLAB/Simulink and experiments based on hardware-in-the-loop (HIL) are conducted. Finally, conclusions are given in Section VI.

II. Modeling and Transient Synchronization Behavior of GFM-WECS

A. Description of GFM-WECS

As shown in Fig. 1, GFM-WECS mainly incorporates a PMSG-based wind turbine (WT), a back-to-back converter, a transmission line, and a control system. SPWM represents the sinusoidal pulse width modulation. PCC represents the point of common coupling. The major difference between the traditional PMSG-based WECS and GFM-WECS lies in the GSC control scheme. Specifically, the phase angle of GFM-WECS is no longer acquired by PLL; instead, it can be obtained through the DVSC method. In addition, the *Q-E* droop control and voltage-current double loop control in [20] and [21] are employed in this paper. The current limiter is also adopted to avoid the overcurrent of the GSC under grid fault. Moreover, the transient response speeds of inner current loop and voltage loop are much faster than those of outer power control loop. Consequently, most literatures ignore the effects of the control loop interactions on the transient stability of GFM-WECS [19], [22]-[24]. Therefore, this paper assumes that the inner control loops in the MSC and GSC controllers are ideal.

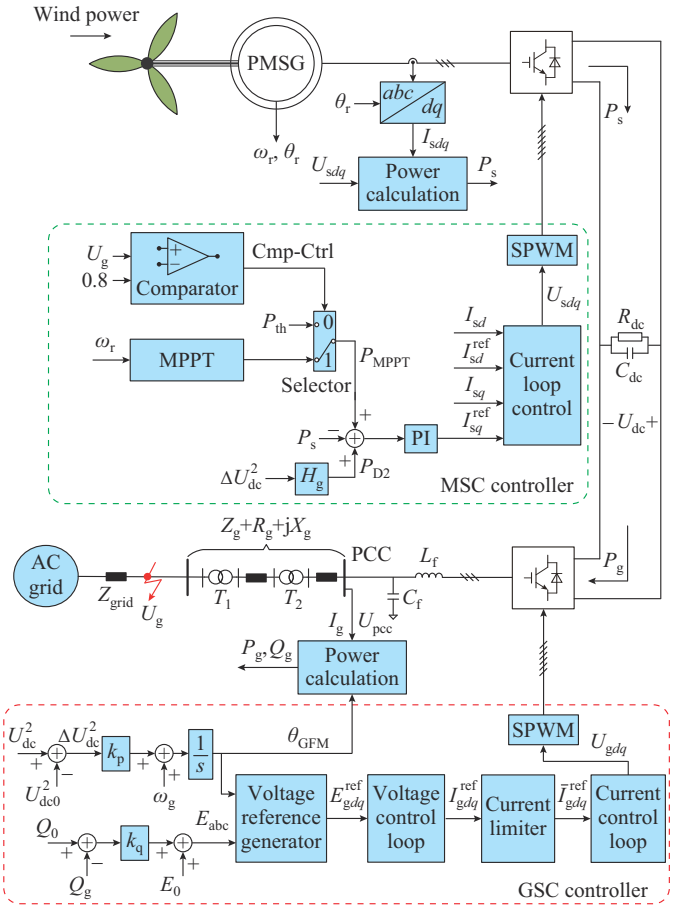

Fig. 1. Block diagram of GFM-WECS under symmetrical grid fault.

In [25], [26], the function of DC-link voltage regulation is mostly out of consideration. This is because the integration of DC-link voltage control will increase the order of the con-

trol loop, and lead to lagged control response and complicated parameter tuning. By contrast, the DVSC method can synchronize GFM-WECS with the power grid while maintaining the DC-link voltage control. Meanwhile, the order of the control loop remains unchanged. Furthermore, it is worth noting that the activated DC chopper may lead to the failure of the DVSC method. Thus, this paper assumes that the voltage fluctuations in the DC-link are effectively kept within the threshold and the DC-link voltage will not be clamped by the chopper. Besides, in general, the DC-link voltage threshold is set between 1.1 p.u. and 1.2 p.u. [27]-[29]. The synchronization of GFM-WECS with the AC power grid can be derived as:

$$\omega_{\mathrm{GFM}}=\omega_{\mathrm{g}}+k_{\mathrm{p}}\left(U_{\mathrm{dc}}^{2}-U_{\mathrm{dc0}}^{2}\right) \tag{1}$$

It can be observed from Fig. 1 that the equivalent power angle δ and its differential of the system are shown as:

$$\begin{cases}\delta=\theta_{\mathrm{GFM}}-\theta_{\mathrm{g}}\\ \dfrac{\mathrm{d}\delta}{\mathrm{d}t}=k_{\mathrm{p}}\Delta U_{\mathrm{dc}}^{2}\end{cases} \tag{2}$$

where $\Delta U_{\mathrm{dc}}^{2}=U_{\mathrm{dc}}^{2}-U_{\mathrm{dc0}}^{2}$. During the steady-state operation, GFM-WECS can achieve some control objectives as follows.

1) The DC-link voltage regulation: $U_{\mathrm{dc}}=U_{\mathrm{dc0}}$.
2) Angular frequency response: $\omega_{\mathrm{GFM}}=\omega_{\mathrm{g}}$.
3) Synchronization with the grid: $\delta=\delta_{0}$.

B. Modelling of GFM-WECS

Figure 1 illustrates the relationship among the input active power from MSC P_{s}, the output active power to the grid P_{g}, and the power charged or discharged by DC-link capacitor, which can be presented as:

$$\frac{C_{\mathrm{dc}}}{2}\frac{\mathrm{d}U_{\mathrm{dc}}^{2}}{\mathrm{d}t}=P_{\mathrm{s}}-P_{\mathrm{D1}}-P_{\mathrm{g}} \tag{3}$$

where P_{D1} is equal to $U_{\mathrm{dc}}^{2}/R_{\mathrm{dc}}$; and R_{dc} is typically set to be thousands of ohms [30], [31]. Then, (3) can be adjusted as:

$$\frac{C_{\mathrm{dc}}}{2}\frac{\mathrm{d}U_{\mathrm{dc}}^{2}}{\mathrm{d}t}+\frac{1}{R_{\mathrm{dc}}}\left(U_{\mathrm{dc}}^{2}-U_{\mathrm{dc0}}^{2}\right)=P_{\mathrm{s}}-P_{\mathrm{g}}-\frac{U_{\mathrm{dc0}}^{2}}{R_{\mathrm{dc}}}\approx P_{\mathrm{s}}-P_{\mathrm{g}} \tag{4}$$

For comparison, the swing equation of the traditional SG can be described as:

$$T_{\mathrm{J}}\frac{\mathrm{d}\omega_{\mathrm{SG}}}{\mathrm{d}t}+D_{\mathrm{SG}}\left(\omega_{\mathrm{SG}}-\omega_{0}\right)=P_{\mathrm{M}}-P_{\mathrm{E}} \tag{5}$$

It can be deduced from (4) and (5) that similar inertia and damping characteristics also exist in the DC-link voltage. The inertia coefficient J_{dc} and damping coefficient D_{dc} of U_{dc}^{2} are equal to $C_{\mathrm{dc}}/2$ and $1/R_{\mathrm{dc}}$, respectively. Substituting (4) into (2) yields:

$$\begin{cases}J_{\mathrm{eq}}\dfrac{\mathrm{d}\omega_{\mathrm{GFM}}}{\mathrm{d}t}+D_{\mathrm{eq}}\left(\omega_{\mathrm{GFM}}-\omega_{\mathrm{g}}\right)=P_{\mathrm{s}}-P_{\mathrm{g}}\\ J_{\mathrm{eq}}=\dfrac{C_{\mathrm{dc}}}{2}\\ D_{\mathrm{eq}}=\dfrac{1}{R_{\mathrm{dc}}k_{\mathrm{p}}}\end{cases} \tag{6}$$

It can be easily found that J_{dc} and D_{dc} are proportional to J_{eq} and D_{eq}, with $J_{\mathrm{eq}}=J_{\mathrm{dc}}$ and $D_{\mathrm{eq}}=D_{\mathrm{dc}}/k_{\mathrm{p}}$. Thus, appropriate adjustment of the inertia and damping coefficients of the DC-link voltage is expected to improve the transient response of GFM-WECS.

As shown in Fig. 2, the transmission line impedance acts as a bridge between GFM-WECS and the AC power grid, and the faults occurring on the grid side will affect U_{pcc} and U_{dc} through the line current I_{g}. Therefore, it is necessary to investigate the interactions between GFM-WECS and the AC power grid.

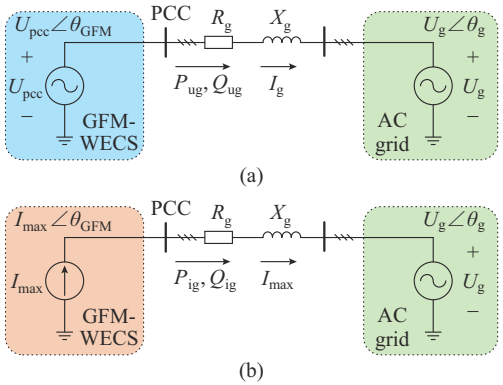

Fig. 2. Equivalent circuit diagram of GFM-WECS. (a) Voltage source operating state. (b) Current source operating state.

The vector diagram between GFM-WECS and the AC power grid is illustrated in Fig. 3. Accordingly, $I_{\mathrm{g}}R_{\mathrm{g}}$ and $I_{\mathrm{g}}X_{\mathrm{g}}$ are the voltage drops of the transmission line resistance and reactance, respectively.

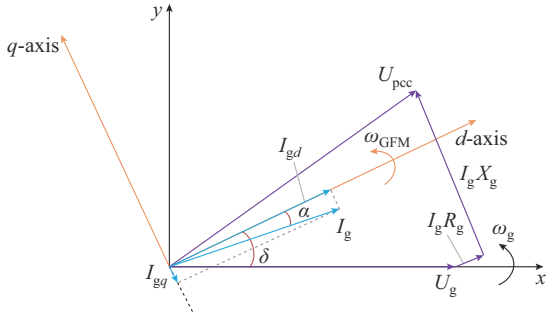

Fig. 3. Vector diagram between GFM-WECS and AC power grid.

In addition, the PCC voltage $\boldsymbol{U}_{\mathrm{pcc}}$ can be represented as:

$$\boldsymbol{U}_{\mathrm{pcc}}=\left(R_{\mathrm{g}}+\mathrm{j}X_{\mathrm{g}}\right)\boldsymbol{I}_{\mathrm{g}}+\boldsymbol{U}_{\mathrm{g}} \tag{7}$$

Then $\boldsymbol{U}_{\mathrm{pcc}}$ is projected onto the d/q-axis rotating frame-based GFM-WECS. As a result, $U_{\mathrm{pcc}d}$ and $U_{\mathrm{pcc}q}$ can be written as:

$$\begin{bmatrix}U_{\mathrm{pcc}d}\\ U_{\mathrm{pcc}q}\end{bmatrix}=\begin{bmatrix}\cos\delta & \sin\delta\\ -\sin\delta & \cos\delta\end{bmatrix}\begin{bmatrix}U_{\mathrm{g}}\\ 0\end{bmatrix}+R_{\mathrm{g}}\begin{bmatrix}I_{gd}\\ I_{gq}\end{bmatrix}+X_{\mathrm{g}}\begin{bmatrix}-I_{gq}\\ I_{gd}\end{bmatrix} \tag{8}$$

where $X_{\mathrm{g}}=\omega_{\mathrm{GFM}}L_{\mathrm{g}}$.

Equation (8) describes the relationship among the PCC voltage, fault grid voltage, and line current, which lays a foundation for calculating the power delivered by GFM-WECS to the power grid. Moreover, considering the capacity constraints of the GSC, it is indispensable for GFM-WECS to implement current limitation controls [15]-[17]. In this paper, the magnitude limiter [16] (also termed as the cir-

cular current limiter [17]) is utilized, and its function can be expressed as:

$$\bar{I}_{gdq}^{\mathrm{ref}}=\begin{cases} I_{gdq}^{\mathrm{ref}} & \left\| I_{gdq}^{\mathrm{ref}} \right\| \le I_{\max} \\ \dfrac{I_{\max}}{\left\| I_{gdq}^{\mathrm{ref}} \right\|} I_{gdq}^{\mathrm{ref}} & \left\| I_{gdq}^{\mathrm{ref}} \right\| > I_{\max} \end{cases} \tag{9}$$

where $I_{\max}$ is set to be 1.5 p.u. [18]. Consequently, it can be observed from Fig. 2(a) and (b) that the power delivered to the power grid can be classified into two categories, depending on whether the line current reaches $I_{\max}$ or not.

Figure 2(a) illustrates the operating state where the output current of GFM-WECS does not reach $I_{\max}$, and GFM-WECS presents a voltage source with a phase angle. The power delivered to the power grid can be obtained as:

$$\begin{cases} P_{\mathrm{ug}}=Y_{\mathrm{eq}}U_{\mathrm{pcc}}U_{\mathrm{g}}\sin(\delta+\alpha)-G_{\mathrm{eq}}U_{\mathrm{g}}^2 \\ Q_{\mathrm{ug}}=Y_{\mathrm{eq}}U_{\mathrm{pcc}}U_{\mathrm{g}}\cos(\delta+\alpha)-B_{\mathrm{eq}}U_{\mathrm{g}}^2 \end{cases} \tag{10}$$

where $Y_{\mathrm{eq}}=\sqrt{G_{\mathrm{eq}}^2+B_{\mathrm{eq}}^2}$; $G_{\mathrm{eq}}=\dfrac{R_{\mathrm{g}}}{R_{\mathrm{g}}^2+X_{\mathrm{g}}^2}$; $B_{\mathrm{eq}}=\dfrac{X_{\mathrm{g}}}{R_{\mathrm{g}}^2+X_{\mathrm{g}}^2}$; and $\alpha=\arctan\left(R_{\mathrm{g}}/X_{\mathrm{g}}\right)$, which is relatively small owing to $R_{\mathrm{g}}<<X_{\mathrm{g}}$.

In comparison, upon reaching $I_{\max}$, GFM-WECS presents a current source with a phase angle and the output current is $I_{\max}$, which is shown in Fig. 2(b). The power delivered to the power grid can be obtained as:

$$\begin{cases} P_{\mathrm{ig}}=U_{\mathrm{g}}I_{\max}\cos(\delta+\alpha)+I_{\max}^2R_{\mathrm{g}} \\ Q_{\mathrm{ig}}=-U_{\mathrm{g}}I_{\max}\sin(\delta+\alpha)+I_{\max}^2X_{\mathrm{g}} \end{cases} \tag{11}$$

Additionally, in accordance with the grid codes (GCs) [32], GFM-WECS should output reactive power to the AC power grid to provide voltage support for the system during LVRT. Moreover, there exists an upper limit for the active power of GFM-WECS and the output active current should be limited [33]. Therefore, the current references I_{gd} and I_{gq} can be presented as:

$$\begin{cases} I_{gq}=1.5\left(0.9-U_{\mathrm{g}}\right) \quad U_{\mathrm{g}}\le 0.8\ \text{p.u.} \\ I_{gd}=\sqrt{0.81-\left(I_{gq}/I_{\max}\right)^2} \end{cases} \tag{12}$$

Subsequently, the output active and reactive power of GFM-WECS during LVRT can be derived as:

$$\begin{cases} P_{\mathrm{g}}\le P_{\mathrm{th}}=U_{\mathrm{g}}\sqrt{0.81-\left(I_{gq}/I_{\max}\right)^2} \\ Q_{\mathrm{g}}\ge Q_{\mathrm{th}}=1.5U_{\mathrm{g}}\left(0.9-U_{\mathrm{g}}\right) \end{cases} \tag{13}$$

Thus, as illustrated in Fig. 1, when U_{g} drops below 0.8 p.u., the comparator in MSC controller outputs a low-level "Cmp-Ctrl" signal, causing the selector to select P_{th} for the MPPT power P_{MPPT}. Moreover, the relationship between P_{s} and P_{MPPT} can be expressed as:

$$P_{\mathrm{s}}=P_{\mathrm{MPPT}}-P_{\mathrm{D2}}=P_{\mathrm{MPPT}}-H_{\mathrm{g}}\Delta U_{\mathrm{dc}}^2 \tag{14}$$

When the output current of GFM-WECS under grid fault does not reach $I_{\max}$, by combining (14) with (4) and (10), (4) can be further rewritten as:

$$\begin{cases} J_{\mathrm{eq}}\dfrac{\mathrm{d}U_{\mathrm{dc}}^2}{\mathrm{d}t}+k_{\mathrm{p}}D_{\mathrm{eq}}\Delta U_{\mathrm{dc}}^2=P_{\mathrm{MPPT}}+G_{\mathrm{eq}}U_{\mathrm{g}}^2-P_{\mathrm{ug,max}}\sin(\delta+\alpha) \\ J_{\mathrm{eq}}=\dfrac{C_{\mathrm{dc}}}{2} \\ D_{\mathrm{eq}}=\dfrac{1}{k_{\mathrm{p}}R_{\mathrm{dc}}}+\dfrac{H_{\mathrm{g}}}{k_{\mathrm{p}}} \\ P_{\mathrm{ug,max}}=Y_{\mathrm{eq}}U_{\mathrm{pcc}}U \end{cases} \tag{15}$$

Therefore, the damping power such as P_{D2} can improve the damping of the DC-link voltage and stabilize GFM-WECS.

According to (1)-(4) and (15), the large-signal equivalent model of GFM-WECS is established, as depicted in Fig. 4. It reveals that the dynamics of the DC-link voltage act as a link between the MSC controller and GSC controller. Besides, there exists similar physical synchronization process in the DC-link voltage to that of SG rotor. When the short-circuit fault occurs, the amplitude of I_{g} will increase and U_{pcc} will decrease instantaneously, leading to fluctuations in U_{dc}. Thus, δ needs to stabilize at a new equilibrium point, which will lead to further changes in P_{g}. Additionally, according to (3) and (14), P_{D1} and P_{D2} are proportional to ΔU_{dc}^2, which indicates that the deeper voltage sag is, the larger ΔU_{dc}^2 will be. It can be concluded that P_{D1} and P_{D2} play roles in decreasing ΔU_{dc}^2 and mitigating the power imbalance between MSC and GSC. Besides, the impacts of key parameters such as D_{eq}, J_{eq}, k_{p}, and Y_{eq} on the transient synchronization process of the DC-Link voltage will be further discussed later.

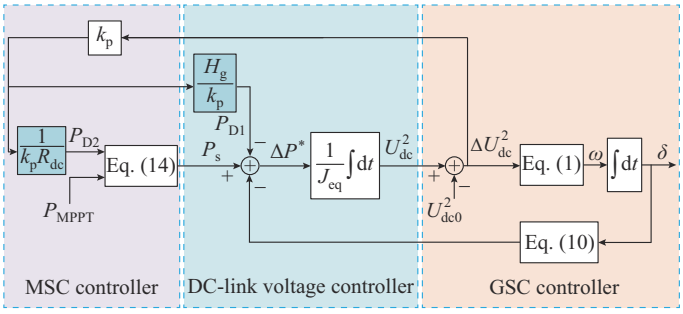

Fig. 4. Block diagram of large-signal equivalent model of GFM-WECS.

C. Impacts of Key Parameters on Transient Synchronization Behavior of GFM-WECS

To better analyze the transient synchronization process of GFM-WECS under symmetrical grid fault, a standardized second-order transfer function based on (1), (2), and (15) can be derived as:

$$\begin{cases} \Delta\omega=\dfrac{\omega_{\mathrm{n}}^2}{s^2+2\xi\omega_{\mathrm{n}}s+\omega_{\mathrm{n}}^2}\dfrac{\Delta P}{P_{\mathrm{ug,max}}} \\ \xi=\dfrac{1/R_{\mathrm{dc}}+H_{\mathrm{g}}}{\sqrt{2k_{\mathrm{p}}C_{\mathrm{dc}}Y_{\mathrm{eq}}U_{\mathrm{pcc}}U_{\mathrm{g}}}} \\ \omega_{\mathrm{n}}=\sqrt{\dfrac{2k_{\mathrm{p}}Y_{\mathrm{eq}}U_{\mathrm{pcc}}U_{\mathrm{g}}}{C_{\mathrm{dc}}}} \end{cases} \tag{16}$$

It can be inferred from (16) that the damping ratio ξ and the resonant frequency ω_n are related to key parameters including k_p, C_{dc}, Y_{eq}, U_{pcc}, U_g, H_g, etc. Therefore, the transient process of GFM-WECS is influenced by various factors such as the control parameters, inertia and damping coefficients, transmission line admittance, and operating conditions of GFM-WECS. Specifically, with the increase of H_g and k_p or decrease of C_{dc} and Y_{eq}, the transient response of GFM-WECS can be improved. Simulations have been carried out to verify the correctness of theoretical analysis, which are shown in Figs. 5 and 6.

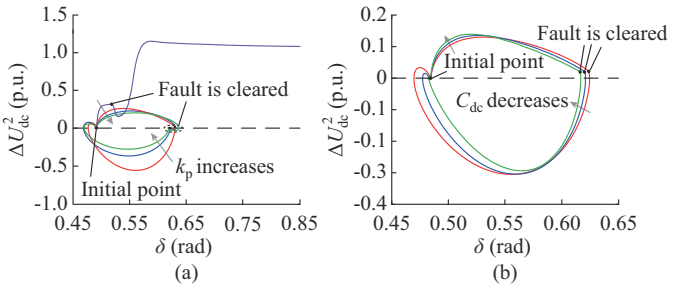

Fig. 5. Phase portrait of GFM-WECS under 0.5 p.u. voltage sag with duration of 200 ms and $SCR=2.5$. (a) $k_p=0.01$, 0.1, 0.2, and 0.3. (b) $C_{dc}=0.05$, 0.1, and 0.15.

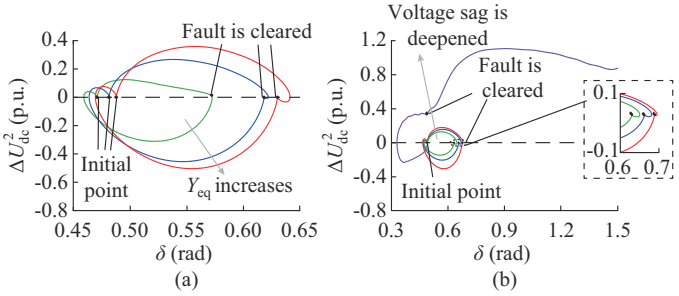

Fig. 6. Phase portrait of GFM-WECS under different voltage sags and SCR with duration of 200 ms. (a) $SCR=2$, 2.5, and 3. (b) $U_g=0.1$ p.u., 0.4 p.u., 0.6 p.u., and 0.8 p.u..

Figure 5 shows the phase portrait of GFM-WECS under 0.5 p.u. voltage sag with duration of 200 ms and $SCR=2.5$. It can be observed that as k_p increases, the instability risk of GFM-WECS decreases and the suppression of the DC-link voltage fluctuations can be achieved gradually. However, an increase in k_p also will lead to an increase in the power angle in Fig. 5(a). By contrast, as C_{dc} decreases, the transient performance of GFM-WECS improves gradually, as shown in Fig. 5(b).

Figure 6(a) depicts that different Y_{eq} means different initial operating points and SEPs. The larger Y_{eq} is, the larger overshoots of the DC-link voltage and the power angle will be. Moreover, Y_{eq} is positively correlated with SCR [8] and a reduction in SCR will deteriorate the transient response of the system. Figure 6(b) shows that with the deepening of the grid fault, the transient behavior of GFM-WECS deteriorates and even experiences transient instability. Besides, the impacts of active power reference P_{MPPT} and current limitation I_{max} on the transient synchronization processes of GFM-WECS have also been explored, as shown in Fig. 7(a) and (b). It is shown that as P_{MPPT} decreases and I_{max} increases, the transient performance of GFM-WECS improves gradually, with smaller overshoots of the DC-link voltage and power angle. Therefore, to improve the transient stability of GFM-WECS under grid fault, the transient characteristics and instability mechanism are essential to be investigated more comprehensively, which will be further studied in Section III.

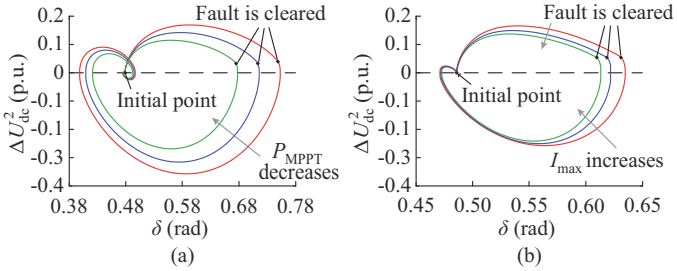

Fig. 7. Phase portrait of GFM-WECS under different active power references and current limitations with duration of 200 ms. (a) $P_{MPPT}=0.4$ p.u., 0.6 p.u., and 0.8 p.u.. (b) $I_{max}=1.3$ p.u., 1.35 p.u., and 1.4 p.u..

III. Transient Synchronization Stability Analysis of GFM-WECS

In this section, the state-space model and the conditions for the existence of equilibrium points (EPs) of GFM-WECS are proposed. Additionally, a novel Lyapunov function considering the damping variation is designed. Furthermore, the DLF and CLF are compared when evaluating the transient stability margin of GFM-WECS.

A. State-space Modeling

Combining (1), (2), and (15), the second-order differential equation of GFM-WECS can be derived as:

$$\ddot{\delta}=\frac{k_p}{J_{eq}}\left(P_{MPPT}+G_{eq}U_g^2\right)-\frac{D_{dc}}{J_{eq}}\dot{\delta}-\frac{k_p}{J_{eq}}G_{eq}U_{pcc}U_g\cos\delta-\frac{k_p}{J_{eq}}B_{eq}U_{pcc}U_g\sin\delta \tag{17}$$

Using the transformation of $x_1=\delta-\delta_s$ and $x_2=\omega-\omega_s$, the state-space model can be represented as:

$$\begin{cases}\dot{x}_1=x_2\\ \dot{x}_2=-Bx_2-f\left(x_1\right)\end{cases} \tag{18}$$

where $f\left(x_1\right)=-A+C\cos\left(x_1+\delta_s\right)+D\sin\left(x_1+\delta_s\right)$. The parameters including A, B, C, and D can be denoted as:

$$\begin{cases}A=\dfrac{k_p}{J_{eq}}\left(P_{MPPT}+G_{eq}U_g^2\right)\\ B=\dfrac{D_{dc}}{J_{eq}}\\ C=\dfrac{k_p}{J_{eq}}G_{eq}U_{pcc}U_g\\ D=\dfrac{k_p}{J_{eq}}B_{eq}U_{pcc}U_g\end{cases} \tag{19}$$

Thus, the EPs under grid fault are expressed as:

$$\begin{cases}\delta_{s1}=\arcsin\left(\dfrac{P_{MPPT}+G_{eq}U_g^2}{Y_{eq}U_{pcc}U_g}\right)-\alpha\\ \delta_{s2}=\pi-\arcsin\left(\dfrac{P_{MPPT}+G_{eq}U_g^2}{Y_{eq}U_{pcc}U_g}\right)-\alpha\end{cases}\tag{20}$$

It can be observed that the EPs of GFM-WECS are mainly relevant to the MPPT power, transmission line admittance, and grid voltage sag. Moreover, the existence of the SEP is essential for GFM-WECS to operate steadily under grid fault. Thus, to evaluate the transient stability margin of GFM-WECS, the region of attraction (ROA) is required to be examined as precisely as possible.

B. Small-signal Stability Analysis

The small-signal stability analysis method is utilized to figure out the EPs and their existence condition. Linearizing (18) around its EP can obtain:

$$\begin{bmatrix}s\Delta x_1\\ s\Delta x_2\end{bmatrix}=\begin{bmatrix}0 & 1\\ C\sin\delta_s-D\cos\delta_s & -B\end{bmatrix}\begin{bmatrix}\Delta x_1\\ \Delta x_2\end{bmatrix}\tag{21}$$

The characteristic polynomial equation of (21) can be represented as:

$$\lambda^2+B\lambda-C\sin\delta_s+D\cos\delta_s=0\tag{22}$$

It can be found that if both $B>0$ and $-C\sin\delta_s+D\cos\delta_s>0$ are satisfied, the real parts of both eigenvalues of λ are negative, and the SEP will exist. Thus, according to (20) and (22), the existence domain of the SEP can be determined by:

$$\begin{cases}-C\sin\delta_s+D\cos\delta_s>0\\ 0<\dfrac{P_{MPPT}+G_{eq}U_g^2}{Y_{eq}U_{pcc}U_g}=\sin(\delta_s+\alpha)<1\end{cases}\tag{23}$$

It can be deduced from (23) that the variation range of the SEP satisfies the inequation, i.e. $-\alpha<\delta_s<\pi/2-\alpha$, and the unstable equilibrium point (UEP) satisfies the inequality, i.e., $\pi/2-\alpha<\delta_s<\pi-\alpha$. Therefore, δ_{s1} and δ_{s2} in (20) are the SEP and UEP, respectively, which is consistent with the EPs depicted in Fig. 8. Consequently, the small-signal analysis method can obtain the existence conditions of EPs, but cannot obtain the ROA of GFM-WECS. Hence, to determine the ROA and evaluate the transient stability margin, the Lyapunov's direct method should be utilized.

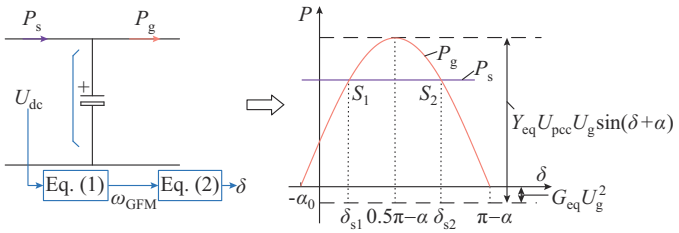

Fig. 8. Power-angle characteristic curve of GFM-WECS under grid fault.

C. Lyapunov's Direct Method

Enlightened by [34], the CLF is represented as V_{CLF} in (24), where the first and second terms on the right represent the kinetic energy and potential energy, respectively.

$$V_{CLF}(x_1,x_2)=\frac{1}{2}x_2^2+\int_0^{x_1}f(\delta)\,\mathrm{d}\delta\tag{24}$$

where $f(\delta)=-A+C\cos\delta+D\sin\delta$. The DLF can be derived as V_{DLF} in (25), where the last term on the right represent the damping energy.

$$V_{DLF}(x_1,x_2)=V_{CLF}(x_1,x_2)+\frac{1}{2}Bx_1\left(\frac{1}{2}Bx_1+x_2\right)\tag{25}$$

The essential conditions for DLF to be an eligible Lyapunov function have been discussed thoroughly in the Supplementary Material A. In addition, the impacts of the damping and inertia coefficients of the DC-link voltage on the ROA of GFM-WECS, as well as CLF and DLF, are discussed in the Supplementary Material B. To further investigate the transient stability margin and determine whether DLF can offer a more reliable stability evaluation result than CLF, time-domain simulations have been conducted, as shown in Fig. 9.

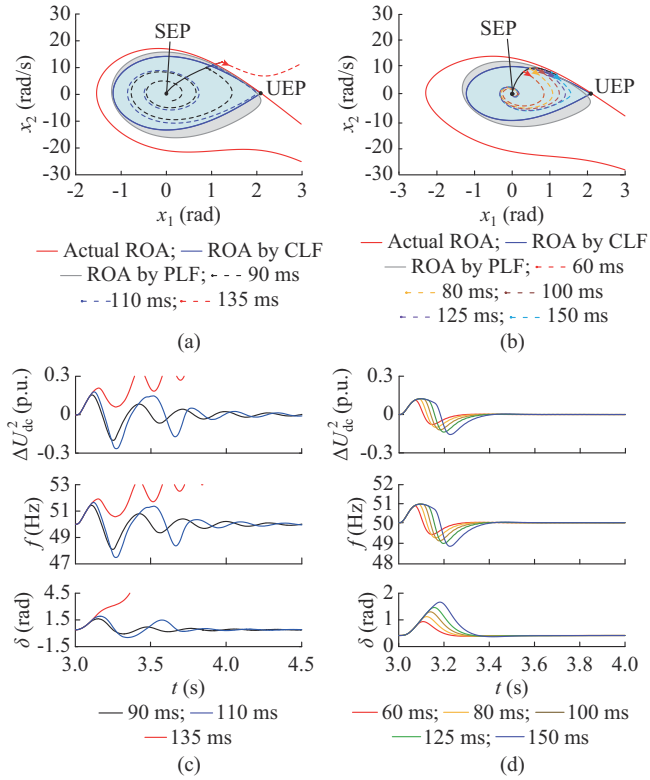

Fig. 9. Comparisons of ROA estimation with CLF and DLF, and time-domain simulation waveforms including ΔU_{dc}^2, f, and δ under different inertia and dampings of DC-link voltage with $SCR=2.1$ and $U_g=0.5$ p.u.. (a) ROA estimation with $J_{dc}=0.025$ and $D_{dc}=0.5$. (b) ROA estimation with $J_{dc}=0.15$ and $D_{dc}=1.4$. (c) Simulation results with $J_{dc}=0.025$ and $D_{dc}=0.5$. (d) Simulation results with $J_{dc}=0.15$ and $D_{dc}=1.4$.

It can be observed from Fig. 9(a) and (c) that when the critical clearing time (CCT) is 90 ms and 110 ms, GFM-WECS can operate steadily finally. The shorter CCT is, the more stable GFM-WECS will be. When CCT is 135 ms, GFM-WECS eventually suffers transient instability, as shown in Fig. 9(a). Moreover, according to the analytical and simulation results in Fig. 9(a) and (c), combined with the Lyapunov function in (24) and (25), the corresponding transient stability evaluation results can be obtained, which are demonstrated in Supplementary Material C. The results

reveal that the conclusions obtained by using DLF for transient stability evaluation are significantly in agreement with the actual situation. By contrast, the stability evaluation results obtained by using CLF are much less accurate. For instance, when CCT reaches 110 ms, the stability evaluation result of CLF is unstable, while GFM-WECS remains stable.

Analytical and simulation results under different inertia and damping coefficients are also illustrated in Fig. 9(b) and (d), and the transient stability evaluation results are demonstrated in the Supplementary Material C. The results indicate that compared with CLF, DLF ensures a more reliable stability evaluation result. In addition, as the inertia and damping coefficients increase, the transient stability evaluation results obtained by DLF are more accurate than those obtained by CLF.

IV. Imapcts of Current Limitation Control on Transient Stability of GFM-WECS

The transient stability analysis above in Section III is based on the condition that the output fault current of GFM-WECS does not reach the current limitation amplitude I_{max}. In this section, the impacts of current limitation on the transient stability of GFM-WECS are investigated.

When the output fault current reaches I_{max}, the current limiter embedded in the control loop of the GSC is triggered. Then, due to different I_{max}, the power-angle characteristic curves distinguish from each other, as shown in Fig. 10. The curves of P_{ug} and P_{ig} are obtained by (10) and (11), respectively. Furthermore, Fig. 10 depicts that there exists an instantaneous change of active power transfer limit [19] P_c at δ_m, which is introduced by the current limiter. It can be deduced that the triggered current limiter can be equivalent to R_v [17], and P_c can be presented as:

$$P_c = P_{ug}(\delta_m) - P_{ig}(\delta_m) = I_{max}^2 R_v \tag{26}$$

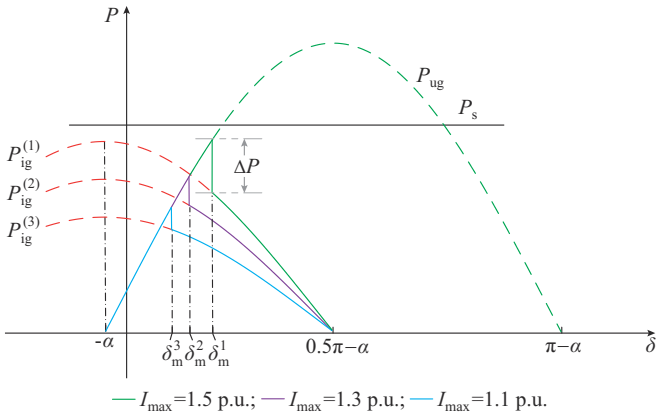

Fig. 10. Power-angle characteristic curves of GFM-WECS under different I_{max}.

where $R_v = \sqrt{\left(U_{pcc}^2 + U_g^2 - 2U_{pcc}U_g\cos\delta\right)/I_{max}^2 - X_g^2}$. Hence, δ_m can be obtained by solving (26), and the implicit solution can be expressed as:

$$f(\delta_m) = \cos 2(\delta_m - \varphi) + 2\frac{U_{pcc}^2 + U_g^2 - 2U_{pcc}U_g\cos\delta_m}{Y_{eq}^2 U_{pcc}^2 U_g^2 + I_{max}^2 U_g^2} - 1 = 0 \tag{27}$$

where $\varphi = \arctan\left(I_{max}/\left(Y_{eq}U_{pcc}\right)\right)$.

To investigate the transient response considering current limitation of GFM-WECS under grid fault, a new second-order differential equation can be further derived as:

$$\ddot{\delta} = -\frac{D_{dc}}{J_{eq}}\dot{\delta} + \frac{k_p}{J_{eq}}\left(P_{MPPT} - U_g I_{max}\cos(\delta+\alpha) - I_{max}^2 R_g\right) \tag{28}$$

The EPs can be obtained by (28), which are denoted as:

$$\begin{cases} \delta_{s1} = -\arccos\left(\dfrac{P_{MPPT} - I_{max}^2 R_g}{U_g I_{max}}\right) - \alpha \\ \delta_{s2} = \arcsin\left(\dfrac{P_{MPPT} - I_{max}^2 R_g}{U_g I_{max}}\right) - \alpha \end{cases} \tag{29}$$

Thus, the stability evaluation index γ considering current limitation can be defined as:

$$\gamma = \delta_m - \delta_s \tag{30}$$

where δ_s refers to δ_{s1}; and γ can be classified into two categories.

1) $\gamma \le 0$, in which no SEP exists and GFM-WECS suffers transient instability.

2) $\gamma > 0$, in which SEP exists, and the larger γ is, the greater the transient stability margin of GFM-WECS will be.

Moreover, according to the relationships among P_s, P_{ig}, and P_{ug}, the influences of P_s on the transient stability can be divided into three categories, i.e., $P_s > P_{ug}(\delta_m)$, $P_{ig}(\delta_m) < P_s < P_{ug}(\delta_m)$, and $P_s < P_{ig}(\delta_m)$, as exemplified in Fig. 11. The yellow and blue areas represent the actual ROA of GFM-WECS with and without current limitation, respectively. It can be concluded from Fig. 11 that the input active power from the MSC, i.e., P_s, determines whether the SEP exists or not.

In addition, as illustrated in Fig. 12, the factors such as the grid voltage sag, current limitation level, and line admittance have a meaningful impact on the transient stability of GFM-WECS under current limitation. Specifically, Fig. 12(a) depicts that the ROA has a tendency to contract as the grid voltage sag deepens. It means that as the grid voltage decreases, the risk of transient instability increases gradually. Figure 12(b) shows that as I_{max} decreases, γ gradually decreases. It implies that the deeper current limitation level is, the lower transient stability margin of the system will be. Figure 12(c) illustrates that the decrease of line admittance will increase the value of γ and expand the ROA. This indicates that GFM-WECS is highly suitable for weak grid scenarios.

In conclusion, when considering the current-limitation control, the effects of the grid voltage sag and line admittance on the transient stability of GFM-WECS are similar to those when the current limitation control is neglected. However, the main difference is that the transient stability margin of GFM-WECS considering current limitation will be greatly decreased. Besides, as the current limitation amplitude decreases, the risk of transient instability increases gradually. It inspires that an improved control strategy should be proposed to enhance the LVRT capability of GFM-WECS during grid fault, which is further investigated in Section V.

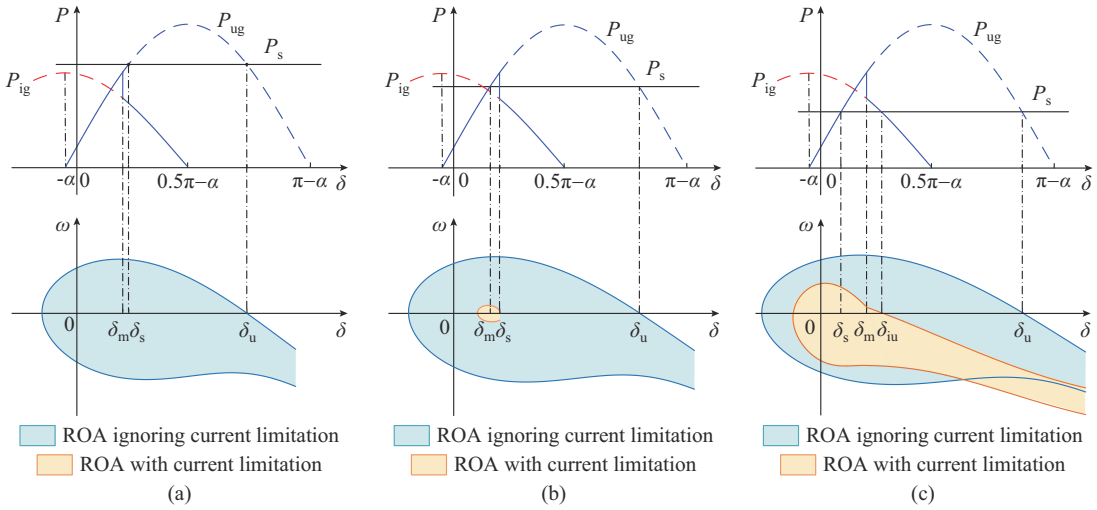

Fig. 11. Influence of P_s on transient stability of GFM-WECS under current limitation. (a) $P_s > P_{ug}(\delta_m)$. (b) $P_{ig}(\delta_m) < P_s < P_{ug}(\delta_m)$. (c) $P_s < P_{ig}(\delta_m)$.

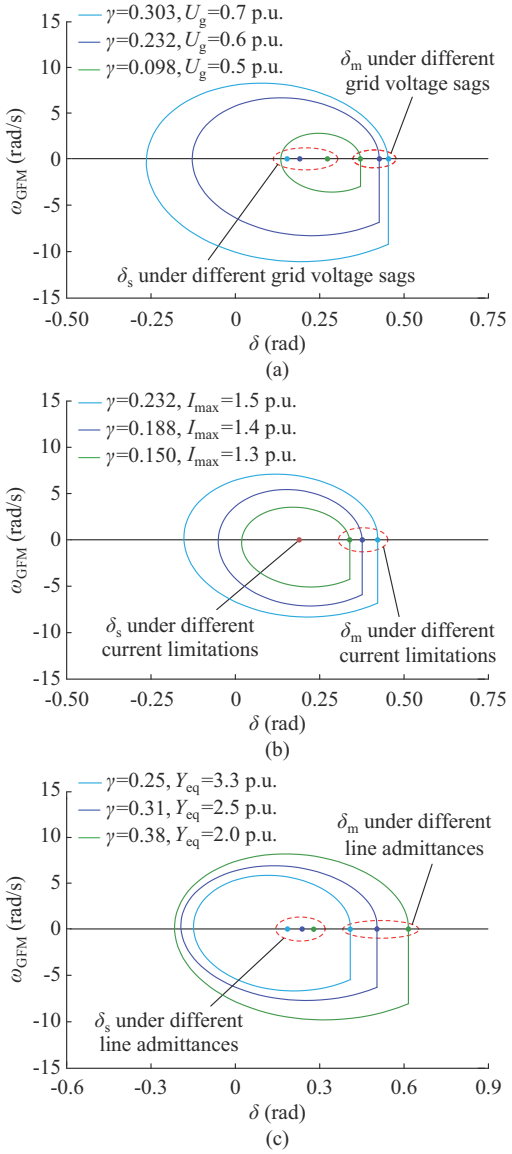

Fig. 12. Impacts of grid voltage sag, current limitation, and line admittance on actual ROA with current limitation. (a) Grid voltage sag. (b) Current limitation. (c) Line admittance.

V. Improved Control Strategy to Enhance Transient Stability of GFM-WECS

Based on the analysis of the above sections, when the grid fault occurs, the insufficient damping aggravates the overshoot of the DC-Link voltage and will lead to a large excursion of the power angle. It deteriorates the transient stability of GFM-WECS, and even causes transient instability.

Consequently, an improved control strategy is proposed in this section to enhance the transient performance of U_{dc} and enhance the transient stability of GFM-WECS under grid fault.

A. Proposed Control Strategy

The block diagram of the proposed control strategy is demonstrated in Fig. 13. It can be found that the MSC control is composed of two control objectives, one is P_{MPPT}, and the other is the feedforward power $H_g\Delta U_{dc}^2$, where $H_s = k_s\Delta U_{dc}^2/U_{dc0}^2$, which aims to reduce the unbalanced power between the MSC and the GSC.

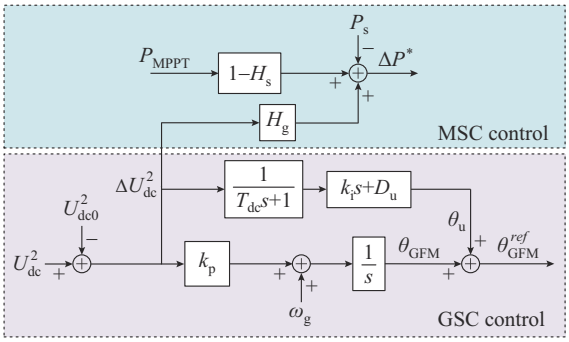

Fig. 13. Block diagram of proposed control strategy.

During grid fault, the input power P_s from the MSC can be denoted as:

$$P_s = \left(1 - k_s\Delta U_{dc}^2/U_{dc0}^2\right)P_{MPPT} - H_g\Delta U_{dc}^2 \tag{31}$$

In terms of the GSC control, it is essentially a phase-shift control strategy through the low-pass filter with T_{dc}. The low-pass filter can minimize the influences of high-order harmon-

ics of the DC-link voltage on the synchronization between GFM-WECS and the AC power grid. Besides, T_{dc} is set to be much smaller than that of GFM-WECS. θ_u is comprised of two parts, which are $k_i s\Delta U_{dc}^2$ and $D_u\Delta U_{dc}^2$, where $D_u = k_t\left|\Delta U_{dc}^2\right|/U_{dc0}^2$. Thus, θ_{GFM}^{ref} can be rewritten as:

$$\theta_{GFM}^{ref} = \theta_{GFM} + \frac{1}{T_{dc}s+1}\left(k_i s\Delta U_{dc}^2 + D_u\Delta U_{dc}^2\right) \tag{32}$$

Assuming θ_u to be relatively small, substituting (31) and (32) into (15) yields:

$$\begin{cases} J_{eq}\dfrac{\mathrm{d}U_{dc}^2}{\mathrm{d}t} + k_p D_{eq}\Delta U_{dc}^2 = P_{MPPT} + G_{eq}U_g^2 - P_{ug,max}\sin(\delta+\alpha) \\ J_{eq} = \dfrac{C_{dc}}{2} + k_i P_{ug,max} \\ D_{eq} = \dfrac{1}{k_p}\left(\dfrac{1}{R_{dc}} + H_g + \dfrac{k_s P_{MPPT}}{U_{dc0}^2} + \dfrac{P_{ug,max}k_t\left|\Delta U_{dc}^2\right|}{U_{dc0}^2}\cos(\delta-\alpha)\right) \end{cases} \tag{33}$$

It can be seen from (33) that the equivalent inertia J_{eq} of GFM-WECS is changed, which raises from $C_{dc}/2$ to $C_{dc}/2 + k_i P_{ug,max}$. Besides, $P_{ug,max}$ is relevant to Y_{eq} and U_g, so J_{eq} can be affected by the line admittance and grid voltage sag. Moreover, the equivalent damping D_{eq} consists of two more parts and is no longer a constant during grid fault. Specifically, when the grid fault occurs, the power imbalance between the MSC and the GSC results in the fluctuations of U_{dc}, and the larger $\left|\Delta U_{dc}^2\right|$ is, the larger D_{eq} will be. Meanwhile, the increased D_{eq} will further reduce the fluctuations in U_{dc} and the last part of D_{eq} is zero when U_{dc} stabilizes at U_{dc0}.

B. Simulation Verification

In order to investigate the transient response of GFM-WECS and the effectiveness of the proposed control strategy under symmetrical grid fault, time-domain simulations based on MATLAB/Simulink are carried out. The parameters used in the time-domain simulations can be found in Supplementary Material D. In addition, the symmetrical grid fault occurs at 1 s with U_g dropping to 0.35 p.u., and the fault is cleared at 2 s.

Firstly, the effectiveness of the proposed control strategy has been verified, as demonstrated in Supplementary Material E. The simulation results show that increasing H_g and k_s in the MSC controller or k_t and k_i in the GSC controller can improve the transient response of GFM-WECS. Besides, compared with relatively strong grid conditions, GFM-WECS under weak grid conditions exhibits better transient stability.

Next, the simulation results for GFM-WECS with different control methods are presented in Fig. 14. It can be found from Fig. 14(b)-(d) that when GFM-WECS operates under the same grid conditions, larger overshoots of U_{dc}, f, and δ appear with the traditional control strategy [35]. However, when the proposed control strategy based on (13) and (33) is adopted, the transient response of GFM-WECS is greatly improved. The results indicate that the proposed control strategy can respond to the dynamics of U_{dc} and adaptively offer more damping support for alleviating the overshoots of U_{dc}, f, and δ. Consequently, the LVRT capability of GFM-WECS is improved. In addition, it can be easily found from Fig. 14(e) and (f) that the output fault current of GFM-WECS with the proposed control method will not reach I_{max}. Besides, Fig. 14(e) and (f) depict the output active and reactive power to the AC power grid. With the proposed control strategy, the output active and reactive power of GFM-WECS during LVRT meet the GCs well according to (12) and (13).

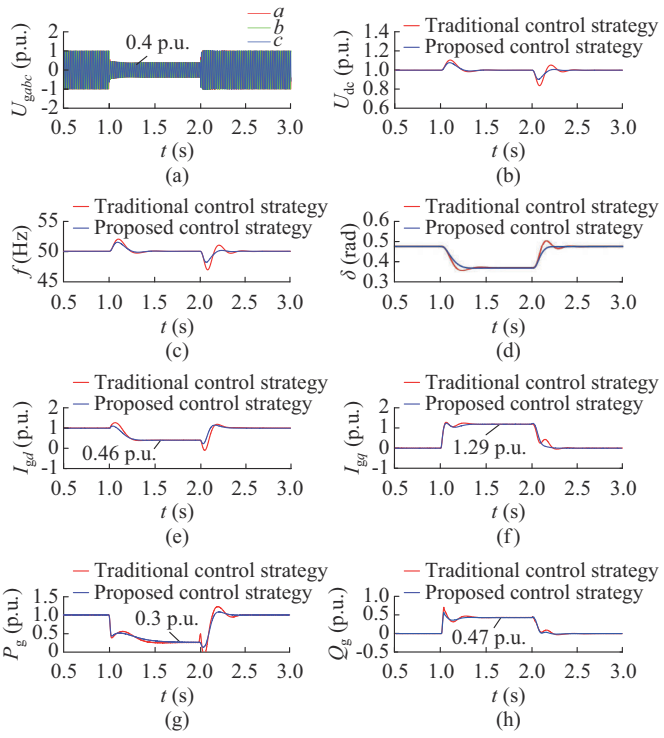

Fig. 14. Transient response of GFM-WECS with $D_{eq}=20$ and $J_{eq}=0.1$ under different control strategies. (a) Three-phase voltage at fault location U_{gabc}. (b) DC-link voltage U_{dc}. (c) System frequency f. (d) Equivalent power angle δ. (e) Output active current I_{gd}. (f) Output reactive current I_{gq}. (g) Output active power P_g. (h) Output reactive power Q_g.

Finally, the validations of GFM-WECS with the proposed control strategy have also been conducted in the IEEE 39-bus 10-machine New England test system, as discussed in the Supplementary Material F. Specifically, in the typical test system, the comparison study of GFL-WECS and GFM-WECS under symmetrical and asymmetrical grid fault is performed and the effects of GFM-WECS on SG are also investigated.

C. HIL Experiment Validation

To further validate the effectiveness of the proposed control strategy, the HIL test rig is founded based on the SpaceR platform, as illustrated in Fig. 15. The main circuit part in Fig. 1 is simulated by the HIL simulator. The controller algorithm in Fig. 1 is carried out in the TI DSP TMS320F2837 7D. All the waveform data are acquired by the oscilloscope. The parameters used in the HIL experiment system are the same as those in the time-domain simulations.

Figure 16 shows the experimental results for GFM-WECS under the same operation conditions but different control strategies. It can be seen from Fig. 16(a) that with the traditional control strategy, the overshoots of U_{dc} and f are 0.07

p.u. and 0.03 p.u., respectively, when the grid fault occurs. Besides, the drops of U_{dc} and f are 0.12 p.u. and 0.07 p.u., respectively, when the fault is cleared. In comparison, when the proposed control strategy is adopted, as shown in Fig. 16(b), both the overshoots and drops of U_{dc} and f are significantly decreased. Compared with the traditional control strategy, the proposed control strategy can respond to the changes of U_{dc} and then adaptively provide more damping support for GFM-WECS during LVRT. Therefore, the proposed control strategy is more favorable for GFM-WECS to maintain its transient stability under grid fault.

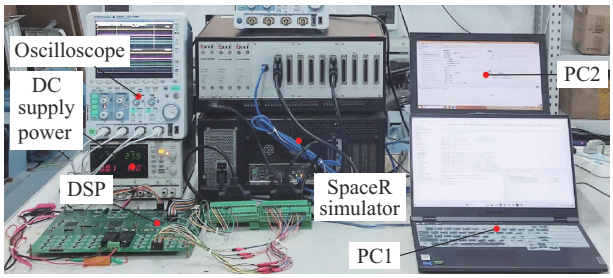

Fig. 15. HIL test rig founded based on SpaceR platform.

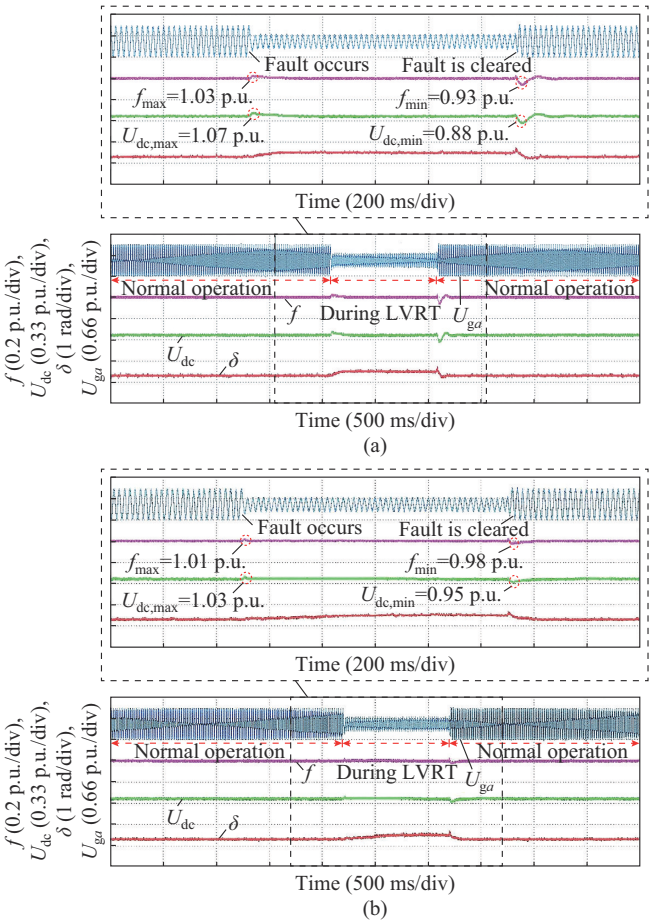

Fig. 16. Transient response of GFM-WECS with D_{eq}=20, J_{eq}=0.1, and U_g=0.35 p.u.. (a) Traditional control strategy. (b) Proposed control strategy.

Figure 17 shows the machine-side, DC-link, and grid-side experimental results of GFM-WECS with the proposed control strategy with U_g=0.4 p.u.. It can be found from Fig. 17(a) that when the grid fault occurs, the A-phase machine-side current i_{sa} decreases to 0.3 p.u., and both the electromagnetic torque T_e and active power P_s decrease to approximately 0.3 p.u., which adheres well to (13). Meanwhile, it can be observed that the reactive power remains around zero throughout the operational phase. Besides, the overshoots of U_{dc} and f are 0.07 p.u. and 0.03 p.u., respectively, which indicates that the transient performance of GFM-WECS with the proposed control strategy under grid fault is enhanced.

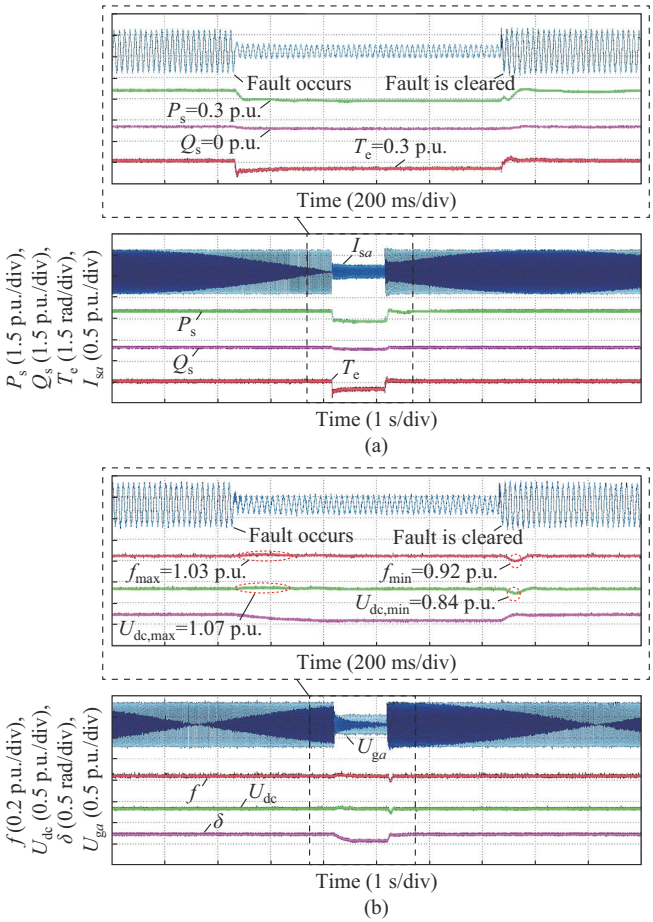

Fig. 17. Transient response of GFM-WECS based on proposed control strategy with D_{eq}=10, J_{eq}=0.1, and U_g=0.4 p.u.. (a) Machine-side simulation results. (b) DC-link and grid-side simulation results.

To validate the influences of SCR and grid voltage sag on the transient response of GFM-WECS, experimental results are obtained in Fig. 18. Figure 18(a) and (b) shows that when SCR is reduced from 2.5 to 1.9, the overshoot of U_{dc} decreases from 0.08 p.u. to 0.05 p.u., and f decreases from 0.034 p.u. to 0.024 p.u.. This indicates that GFM-WECS is more suitable for weak grid scenarios. In addition, it can be seen from Fig. 18(c) that when U_g drops from 1 p.u. to 0.75 p.u., the maximal values of U_{dc} and f are 1.04 p.u. and 1.02 p.u., respectively. By contrast, a more severe grid fault condition is depicted in Fig. 18(d), i.e., U_g drops from 1 p.u. to 0.35 p.u., and the maximal values of U_{dc} and f are 1.12 p.u. and 1.06 p.u., respectively. Hence, it can be concluded that the more severe the grid fault is, the worse the transient stability of GFM-WECS will become, which is consistent with the analytical and simulation results obtained in Section II.

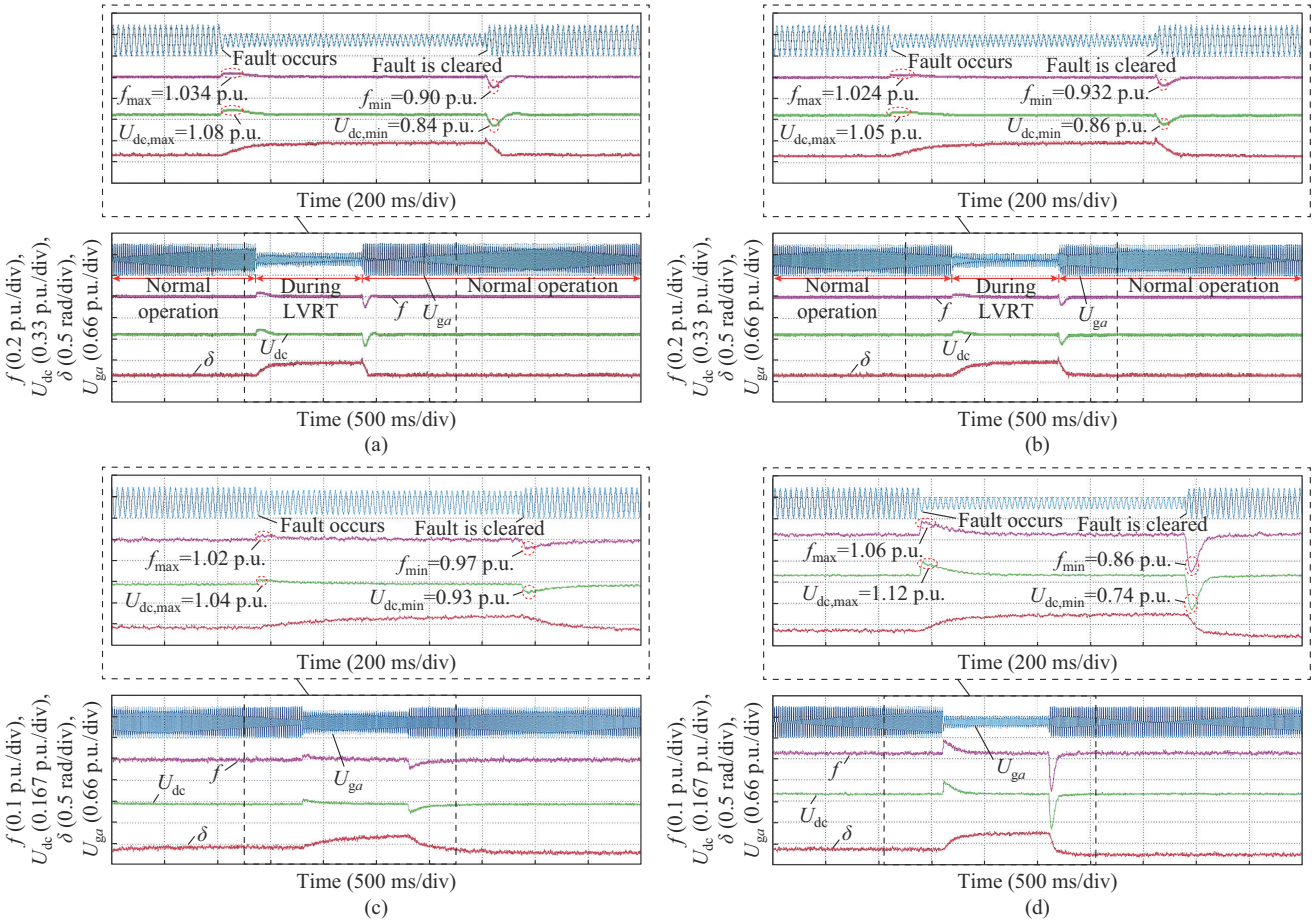

Fig. 18. Transient response of GFM-WECS varying with SCR and grid voltage sags. (a) $SCR = 2.5$. (b) $SCR = 1.9$. (c) U_g=0.75 p.u.. (d) U_g=0.35 p.u..

VI. Conclusion

In this paper, the transient synchronization stability and the impacts of current limitation control on the transient stability margin of GFM-WECS under grid fault are investigated. Then, an improved control strategy is proposed to enhance the transient stability of GFM-WECS under symmetrical grid fault. The following conclusions can be summarized.

1) The dynamic interactions between the MSC and the GSC of GFM-WECS under grid fault are investigated through the established large-signal equivalent model. It can be concluded that the transient stability of GFM-WECS can be improved by applying the damping power in the MSC control. The damping and inertia characteristics of DC-link voltage are similar to those of SG during grid fault.

2) The second-order differential equation of GFM-WECS is derived, and the transient stability is evaluated through DLF. Compared with CLF, DLF can respond to both the changes of inertia and damping coefficients and ensure a more reliable stability evaluation result.

3) The transient stability of GFM-WECS under current limitation is investigated, and the stability evaluation index is developed to estimate the stability margin. When the current limitation control is triggered, the impacts of grid voltage sag and SCR on the transient stability of GFM-WECS are same as when current limitation is neglected, but the stability margin is significantly reduced. Besides, with the deepening of current limitation level, the risk of transient instability increases.

4) An improved control strategy including MSC control and GSC control is proposed. Compared with the conventional control strategy, the proposed control strategy can not only respond to the dynamics of the DC-link voltage, but also adaptively provide more damping support for GFM-WECS during LVRT. Consequently, the transient stability of GFM-WECS is improved considerably.

In summary, the transient synchronization stability and improved control strategy of GFM-WECS under symmetrical grid fault are investigated in this paper. Moreover, to achieve a more comprehensive understanding of the transient stability of GFM-WECS, a comparison study of GFL-WECS and GFM-WECS under both symmetrical and asymmetrical grid faults has been conducted. However, due to space limitations of this paper, a systematic exploration of diverse asymmetrical fault scenarios and the potential for induced synchronization instability has not been conducted, which will be further studied in the future.

References

[1] J. Zhao, Z. Wu, H. Long *et al.*, "Optimal operation control strategies for active distribution networks under multiple states: a systematic review," *Journal of Modern Power Systems and Clean Energy*, vol. 12, no. 5, pp. 1333-1344, Sept. 2024.

[2] Z. Wang, K. Zhuang, Y. Wang *et al.*, "Transient stability analysis of

WTs based on VSG-PMSG considering the machine-side dynamics," in *Proceedings of 2023 3rd Power System and Green Energy Conference (PSGEC)*, Shanghai, China, Aug. 2023, pp. 105-109.
[3] J. Pei, J. Yao, R. Liu *et al*., "Characteristic analysis and risk assessment for voltage-frequency coupled transient instability of large-scale grid-connected renewable energy plants during LVRT," *IEEE Transactions on Industrial Electronics*, vol. 67, no. 7, pp. 5515-5530, Jul. 2020.
[4] J. L. Rodríguez-Amenedo, S. A. Gómez, M. Zubiaga *et al*., "Grid-forming control of voltage source converters based on the virtual-flux orientation," *IEEE Access*, vol. 11, pp. 10254-10274, Jan. 2023.
[5] Y. Ma, L. Tao, X. Zhou *et al*., "Analysis and control of fault ride-through capability improvement for wind energy conversion system using linear active disturbance rejection control with correction link," *IEEE Access*, vol. 8, pp. 73816-73827, Apr. 2020.
[6] N. Jabbour, E. Tsioumas, C. Mademlis *et al*., "A highly effective fault-ride-through strategy for a wind energy conversion system with a doubly fed induction generator," *IEEE Transactions on Power Electronics*, vol. 35, no. 8, pp. 8154-8164, Aug. 2020.
[7] S. Huang, J. Yao, J. Pei *et al*., "Transient synchronization stability improvement control strategy for grid-connected VSC under symmetrical grid fault," *IEEE Transactions on Power Electronics*, vol. 37, no. 5, pp. 4957-4961, May 2022.
[8] Y. Liu, J. Yao, J. Pei *et al*., "Transient stability enhancement control strategy based on improved PLL for grid connected VSC during severe grid fault," *IEEE Transactions on Energy Conversion*, vol. 36, no. 1, pp. 218-229, Mar. 2021.
[9] Z. Lv, C. Zhang, Y. Zhang *et al*., "Quantitative transient synchronization stability margin analysis of PLL-based VSC considering LVRT control strategy," in *Proceedings of 2023 IEEE 14th International Symposium on Power Electronics for Distributed Generation Systems (PEDG)*, Shanghai, China, Jun. 2023, pp. 709-715.
[10] T. Lin, M. Das, A. Gole *et al*., "Adaptive fault ride through control of VSM grid-forming converters," *Electric Power Systems Research*, vol. 223, p. 109606, Oct. 2023.
[11] J. Lei, X. Xiang, Q. Qu *et al*., "The analysis and calculation of power angle transient characteristics in VSG control using parameter-perturbation-based averaging method," *IEEE Transactions on Industrial Electronics*, vol. 70, no. 10, pp. 10249-10260, Oct. 2023.
[12] S. Chen, J. Yao, J. Pei *et al*., "Transient stability analysis and improved control strategy for DC-link voltage of DFIG-based WT during LVRT," *IEEE Transactions on Energy Conversion*, vol. 37, no. 2, pp. 880-891, Jun. 2022.
[13] K. Zhuang, Z. Wang, D. Sun *et al*., "Transient stability analysis and coordination control design for grid-forming PMSG based on dynamics of dc-link capacitor," in *Proceedings of 2023 IEEE PES General Meeting*, Orlando, USA, Jul. 2023, pp. 1-5.
[14] X. Yuan, Z. Du, Y. Li *et al*., "Energy function-based analysis of PMSG-based WT with DC voltage synchronization control," in *Proceedings of 2021 IEEE PES General Meeting*, Washington DC, USA, Jul. 2021, pp. 1-5.
[15] H. Zhang, W. Xiang, W. Lin *et al*., "Grid forming converters in renewable energy sources dominated power grid: control strategy, stability, application, and challenges," *Journal of Modern Power Systems and Clean Energy*, vol. 9, no. 6, pp. 1239-1256, Nov. 2021.
[16] B. Fan, T. Liu, F. Zhao *et al*., "A review of current-limiting control of grid-forming inverters under symmetrical disturbances," *IEEE Open Journal of Power Electronics*, vol. 3, pp. 955-969, Dec. 2022.
[17] B. Fan and X. Wang, "Equivalent circuit model of grid-forming converters with circular current limiter for transient stability analysis," *IEEE Transactions on Power Systems*, vol. 37, no. 4, pp. 3141-3144, Jul. 2022.
[18] P. Ge, F. Xiao, C. Tu *et al*., "Comprehensive transient stability enhancement control of a VSG considering power angle stability and fault current limitation," *CSEE Journal of Power and Energy Systems*, to be published, doi: 10.17775/CSEEJPES.2021.00340
[19] G. Wang, L. Fu, Q. Hu *et al*., "Transient synchronization stability of grid-forming converter during grid fault considering transient switched operation mode," *IEEE Transactions on Sustainable Energy*, vol. 14, no. 3, pp. 1504-1515, Jul. 2023.
[20] B. Wu, Z. Gao, X. Zhou *et al*., "Research and simulation of DC microgrid three-phase AC-DC converter control strategy based on double loop," *IEEE Access*, vol. 8, pp. 186448-186461, Oct. 2020.
[21] Z. Wang, Y. Wang, M. Davari *et al*., "An effective PQ-decoupling control scheme using adaptive dynamic programming approach to reducing oscillations of virtual synchronous generators for grid connection with different impedance types," *IEEE Transactions on Industrial Electronics*, vol. 71, no. 4, pp. 3763-3775, Apr. 2024.
[22] R. Vijayapriya, P. Raja, and M. P. Selvan, "A modified active power control scheme for enhanced operation of PMSG-based WGs," *IEEE Transactions on Sustainable Energy*, vol. 9, no. 2, pp. 630-638, Apr. 2018.
[23] H. Xu, C. Wang, Z. Wang *et al*., "Stability analysis and enhanced virtual synchronous control for brushless doubly-fed induction generator based wind turbines," *Journal of Modern Power Systems and Clean Energy*, vol. 12, no. 5, pp. 1445-1458, Sept. 2024.
[24] M. Zhao, X. Yuan, J. Hu *et al*., "Voltage dynamics of current control time-scale in a VSC-connected weak grid," *IEEE Transactions on Power Systems*, vol. 31, no. 4, pp. 2925-2937, Jul. 2016.
[25] Y. Peng, Z. Shuai, C. Shen *et al*., "Transient stabilization control of electric synchronous machine for preventing the collapse of dc-link voltage," *IEEE Transactions on Smart Grid*, vol. 14, no. 1, pp. 82-93, Jan. 2023.
[26] M. M. Rahman and Y. A.-R. I. Mohamed, "Interaction dynamics and active suppression of instability in parallel photovoltaic voltage-and current-source converters connected to a weak grid," *IEEE Open Journal of Power Electronics*, vol. 4, pp. 395-414, May 2023.
[27] A. Uehara, A. Pratap, T. Goya *et al*., "A coordinated control method to smooth wind power fluctuations of a PMSG-based WECS," *IEEE Transactions on Energy Conversion*, vol. 26, no. 2, pp. 550-558, Jun. 2011.
[28] Q. Zhang, J. He, Y. Xu *et al*., "Average-value modeling of direct-driven PMSG-based wind energy conversion systems," *IEEE Transactions on Energy Conversion*, vol. 37, no. 1, pp. 264-273, Mar. 2022.
[29] S. B. Naderi, M. Negnevitsky, and K. M. Muttaqi, "A modified DC chopper for limiting the fault current and controlling the DC-link voltage to enhance fault ride-through capability of doubly-fed induction-generator-based wind turbine," *IEEE Transactions on Industry Applications*, vol. 55, no. 2, pp. 2021-2032, Mar.-Apr. 2019.
[30] M. Davari and Y. A.-R. I. Mohamed, "Robust DC-link voltage control of a full-scale PMSG wind turbine for effective integration in DC grids," *IEEE Transactions on Power Electronics*, vol. 32, no. 5, pp. 4021-4035, May 2017.
[31] C. Arghir, T. Jouini, and F. Dörfler, "Grid-forming control for power converters based on matching of synchronous machines," *Automatica*, vol. 95, pp. 273-282, Sept. 2018.
[32] *Technical Rule for Connecting Wind Farm to Power System*, GB/T 19963.1-2021, 2021.
[33] Y. Khayat, P. Chen, M. Bongiorno *et al*., "FRT capability of grid-forming power converters: an antiwindup scheme," *IEEE Transactions on Power Electronics*, vol. 39, no. 10, pp. 12842-12855, Oct. 2024.
[34] Y. Li, Y. Tang, Y. Lu *et al*., "Synchronization stability of grid-connected VSC with limits of PLL," *IEEE Transactions on Power Systems*, vol. 38, no. 4, pp. 3965-3976, Jul. 2023.
[35] L. Huang, H. Xin, Z. Wang *et al*., "A virtual synchronous control for voltage-source converters utilizing dynamics of DC-link capacitor to realize self-synchronization," *IEEE Journal of Emerging and Selected Topics in Power Electronics*, vol. 5, no. 4, pp. 1565-1577, Dec. 2017.

Hai Xie received the B.Eng. degree in electrical engineering and automation from Taiyuan University of Technology, Taiyuan, China, in 2022. He is currently working toward the M.S. degree in electrical engineering with the School of Electrical Engineering, Chongqing University, Chongqing, China. His research interests include large-disturbance stability analysis of wind energy conversion system and grid-forming control.

Jun Yao received the B.Eng., M.Sc., and Ph.D. degrees in electrical engineering from Chongqing University, Chongqing, China, in 2001, 2004, and 2007, respectively. Since 2004, he has been with the School of Electrical Engineering, Chongqing University, where he is currently a Professor. From January 2012 to January 2013, he was a Visiting Researcher at the Department of Energy Technology, Aalborg University, Aalborg, Denmark. His research interests include electric machine, power electronics conversion and control, renewable power generation, and wind energy and power electronics application in power system.

Wenwen He received the B.Eng. degree in electrical engineering and automation from China University of Mining and Technology, Xuzhou, China, in 2021, and the M.Sc. degree in electrical engineering from the School of Electrical Engineering, Chongqing University, Chongqing, China, in 2024. His research interests include transient stability analysis and control of virtual synchronous generator.

Dong Yang received the B.Eng. degree in electrical engineering and automation from Yanshan University, Qinhuangdao, China, in 2022. He is currently working toward the Ph.D. degree with the School of Electrical Engineering, Chongqing University, Chongqing, China. His research interests include control of stability of power system and renewable power generation.

Sheng Gong received the B.Eng. degree in electrical engineering and automation from Jiangsu University, Zhenjiang, China, in 2021. He is currently working toward the Ph.D. degree with the School of Electrical Engineering, Chongqing University, Chongqing, China. His research interests include stability control of power system and renewable power generation.

Linsheng Zhao received the B.Eng. degree in electrical engineering and automation from Anhui University, Hefei, China, in 2023. He is currently working toward the M.Sc. degree in electrical engineering with the School of Electrical Engineering, Chongqing University, Chongqing, China. His research interests include influence of wind power integration on power system stability, and control of wind power generation system.